

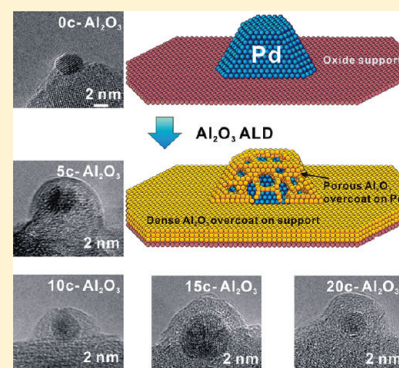
Porous Alumina Protective Coatings on Palladium Nanoparticles by Self-Poisoned Atomic Layer Deposition

Junling Lu,[†] Bin Liu,[‡] Jeffrey P. Greeley,[‡] Zhenxing Feng,[‡] Joseph A. Libera,[†] Yu Lei,[†] Michael J. Bedzyk,[‡] Peter C. Stair,^{§,#} and Jeffrey W. Elam^{*,†}[†]Energy Systems Division, [‡]Center for Nanoscale Materials, and [§]Chemical Sciences & Engineering Division, Argonne National Laboratory, Argonne, Illinois 60439, United States[‡]Department of Materials Science and Engineering and [#]Department of Chemistry, Northwestern University, Evanston, Illinois 60208, United States

S Supporting Information

ABSTRACT: Atomic layer deposition (ALD) of Al₂O₃ using trimethylaluminum (TMA) and water on Pd nanoparticles (NPs) was studied by combining in situ quartz crystal microbalance (QCM) measurements, in situ quadrupole mass spectrometry (QMS), and transmission electron microscopy (TEM) with density functional theory (DFT) calculations. TEM images of the ALD Al₂O₃ overcoated Pd showed conformal Al₂O₃ films on the Pd NPs as expected for ALD. However, hydrogen detected by in situ QMS during the water pulses suggested that the ALD Al₂O₃ films on the Pd NPs were porous rather than being continuous coatings. Additional in situ QCM and QMS measurements indicated that Al₂O₃ ALD on Pd NPs proceeds by a self-poisoning, self-cleaning process. To evaluate this possibility, DFT calculations were performed on Pd(111) and Pd(211) as idealized Pd NP surfaces. These calculations determined that the TMA and water reactions are thermodynamically favored on the stepped Pd(211) surface, consistent with previous observations. Furthermore, the DFT studies identified methylaluminum (AlCH₃^{*}, where the asterisk designates a surface species) as the most stable intermediate on Pd surfaces following the TMA exposures, and that AlCH₃^{*} transforms into Al(OH)₃^{*} species during the subsequent water pulse. The gas phase products observed using in situ QMS support this TMA dissociation/hydration mechanism. Taken together, the DFT and experimental results suggest a process in which the Pd surface becomes poisoned by adsorbed CH₃^{*} species during the TMA exposures that prevent the formation of a complete monolayer of adsorbed Al species. During the subsequent H₂O exposures, the Pd surface is cleaned of CH₃^{*} species, and the net result is a porous Al₂O₃ film. This porous structure can retain the catalytic activity of the Pd NPs by providing reagent gases with access to the Pd surface sites, suggesting a promising route to stabilize active Pd catalysts.

KEYWORDS: atomic layer deposition, supported metal catalyst, palladium nanoparticle, stabilization, alumina, growth mechanism, density functional theory



■ INTRODUCTION

Atomic layer deposition (ALD) was developed in the late 1970s to meet the requirements for the growth of large-area thin films for electroluminescent, flat-panel displays.^{1,2} ALD relies on self-limiting sequential binary reactions between gaseous precursor molecules and a substrate to deposit films in an atomic layer-by-layer fashion. An inert gas purge period is introduced between each precursor pulse to prevent mixing of the chemicals, which would cause non self-limiting growth.^{2–4} Because of the unique feature of self-limiting growth in each deposition cycle, ALD can deposit uniform and conformal coatings regardless of whether the substrate is flat or possesses high aspect ratio features, high surface area, or high porosity.^{3,5–9} As a consequence, ALD has attracted great attention and applications have extended far beyond microelectronics into fields such as catalysis,^{10–17} photovoltaics,^{18–21} batteries,²² fuel cells,^{16,23} polymers,^{3,24,25} and microdevices.^{26,27}

For catalytic applications, well-dispersed and uniform metal nanoparticles (NPs) have been successfully prepared using ALD with precise particle size control.^{28–31} These ALD metal NPs often showed comparable or better catalytic performance than those synthesized by conventional methods, such as impregnation, ion-exchange, and deposition-precipitation.^{11,12,14,16} Recently, there have been a number of attempts to stabilize supported metal NPs using ALD metal oxide coatings.^{13,17,32–34} These studies were motivated by the atomically precise control over the thickness and composition of the protective layers afforded by ALD in comparison with other methods such as chemical vapor deposition, grafting, microemulsion, and dendrimer encapsulation.^{35–41} These less

Received: January 18, 2012

Revised: April 11, 2012

Published: May 8, 2012

precise methods can yield overly thick protective shells that impede mass transport and reduce catalytic performance.

Al₂O₃ ALD performed using TMA and water is one of the most successful ALD procedures, and has been extensively investigated.^{4,42–45} The mechanism of Al₂O₃ ALD on oxide surfaces is well understood: first, TMA reacts with hydroxyl groups on the starting surface forming Al(CH₃)_x* ($x = 1–2$, where the asterisk designates a surface species) and CH₄ (Figure 1a); next, the Al(CH₃)_x* terminated surface transforms

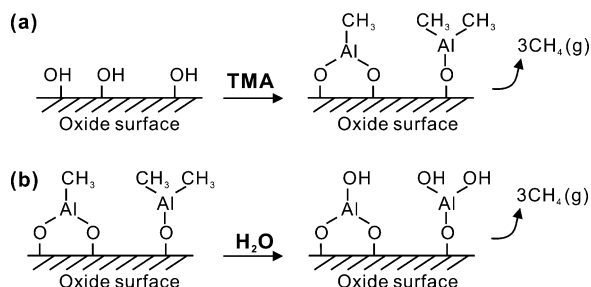


Figure 1. Schematic illustration of one Al₂O₃ ALD cycle on a metal oxide surface. (a) TMA reacts with surface hydroxyl groups liberating methane; (b) water reacts with the Al(CH₃)_x-terminated surface forming methane and regenerating the hydroxylated surface.

to an Al(OH)_x* ($x = 1–2$) terminated surface after the following H₂O exposure and again releases CH₄ (Figure 1b).^{4,44,45} In situ quartz crystal microbalance (QCM) measurements performed during Al₂O₃ ALD demonstrated that the ratio of the total mass gain in one ALD cycle (Δm_0) to the mass gain after the TMA pulse (Δm_1) is $\Delta m_0/\Delta m_1 \approx 1.1$, which implies $x = 1.6$ according to the mechanism of Figure 1.^{4,44,46} Highly linear growth rates of 1.1–1.3 Å/cycle were measured on planar surfaces using spectroscopic ellipsometry, with the lower values occurring at higher temperatures where the surface hydroxyl coverage is reduced.^{4,42,43,47}

Although the mechanism for Al₂O₃ ALD on oxide surfaces requires surface hydroxyls, Al₂O₃ ALD can also be grown on noble metal surfaces. For instance, Zhang et al. demonstrated that a subnanometer thick ALD Al₂O₃ layer coated on silver film-overnanosphere (AgFON) substrates can maintain and stabilize the activity of the underlying silver for surface-enhanced Raman spectroscopy (SERS).^{33,48} Based on X-ray photoelectron spectroscopy and in situ QCM results, Whitney et al. suggested that the Al₂O₃ ALD initiates when TMA decomposes on the Ag surface.⁴⁹ In a different study, Liang et al. prepared aluminum alkoxide (alucone) hydride films on Pt surfaces using alternating exposures to TMA and ethylene glycol (EG) and thermally decomposing these films to form highly porous Al₂O₃.³⁴ Pt/SiO₂ catalysts coated with these porous, ultrathin alumina layers were very stable when calcined in air at 1073 K. The 20-cycle alucone-coating (about 1.2 nm) reduced the catalytic activity of the Pt NPs in CO oxidation reactions. This is likely due to the small pore size in the alumina layer.³⁴

We recently utilized ALD Al₂O₃ protective layers with precise thicknesses to inhibit the sintering of supported nanosized ALD Pd catalysts in the methanol decomposition reaction carried out at elevated temperatures.¹³ Up to a certain thickness, the Al₂O₃ protective layers preserved or even slightly enhanced the catalytic activity. Using CO as a probe molecule, we found that the ALD Al₂O₃ overcoats preferentially nucleate at corners, steps, and edges of the Pd NPs while leaving the

Pd(111) facets accessible for methanol conversion, and this site preference became more pronounced after reaction testing. Thicker Al₂O₃ overcoats (with thicknesses of ~8 nm) were further tested on supported Pd catalysts and found to effectively prevent the catalyst deactivation through either sintering or coking in excess of the Tammann temperature.¹⁷ These remarkable improvements in catalytic performance were again suggested mainly due to the preferential blocking of the more reactive low-coordination Pd sites by the Al₂O₃ overcoat.

Although significant improvements in catalytic performance can be achieved by applying ALD Al₂O₃ overcoats onto Pd, the mechanism for Al₂O₃ ALD on Pd surfaces is unknown. In this work, we have investigated Al₂O₃ ALD on Pd surfaces with in situ QCM, in situ quadrupole mass spectrometry (QMS), and transmission electron microscopy (TEM). In particular, we sought to understand how the catalytic activity of the Pd NPs was maintained even after many ALD Al₂O₃ cycles that would be expected to bury the Pd surface. Density functional theory (DFT) calculations were also adopted to further elucidate the details of TMA adsorption and the subsequent hydration process on both Pd(111) and Pd(211) surfaces.

EXPERIMENTAL SECTION

ALD Reactor. ALD was performed in a viscous flow stainless steel tube reactor system.⁴⁶ Ultrahigh purity nitrogen (99.999%) carrier gas continuously passed through the tube reactor at a mass flow rate of 300 sccm and a pressure of 1 Torr. The ALD reactor was equipped with a quadrupole mass spectrometer (QMS, Stanford Research Systems RGA300) located downstream of the flow tube in a differentially pumped chamber separated from the reactor tube by a 35 μm orifice and evacuated using a 50 L/s turbomolecular pump. A quartz crystal microbalance (QCM) was mounted in a commercial QCM housing modified to allow a nitrogen purge that prevents growth on the back of the sensor. The QCM was installed in the middle of reaction tube for in situ monitoring of the ALD.

Al₂O₃ and Pd ALD. Al₂O₃ ALD was carried out by alternately dosing TMA (Sigma-Aldrich, 97%) and deionized water at 473 K. Pd ALD was performed by alternately dosing Pd(II) hexafluoroacetylacetonate (Pd(hfac)₂, Sigma-Aldrich, > 97%) and formalin at 473 K. The Pd(hfac)₂ precursor was contained in a stainless steel bubbler heated to 333 K to increase the vapor pressure.^{28,50} Ultrahigh purity nitrogen with a flow rate of 50 sccm passed through the bubbler and carried the Pd(hfac)₂ precursor to the reaction chamber. Formalin is a solution of 37% formaldehyde in water with 10–15% methanol added as a stabilizer. The precursor inlet lines were heated to 423 K to prevent condensation of the ALD precursors. To define the ALD cycles, the first precursor pulse time, the first nitrogen purge time, the second precursor pulse time, and the second nitrogen purge time are expressed as $t_1-t_2-t_3-t_4$, in seconds (s).

In situ QCM and QMS Measurements. In situ QCM and QMS measurements were performed to study the Al₂O₃ growth on Pd surfaces and to monitor the reaction products evolved during each half ALD cycle, respectively. Prior to these measurements, 300 ALD Al₂O₃ cycles were performed using the timing sequence 1–5–1–5 to deposit ~30 nm Al₂O₃ on the QCM sensor as well as on the inner surfaces of the ALD reactor that generate a majority of the species detected by the QMS. Next, 150 ALD Pd cycles were performed using the timing sequence 2–2–2–2 to deposit a high density of Pd NPs.⁵⁰ After preparing the supported Pd NPs, 50 ALD Al₂O₃ overcoating cycles were performed using the timing sequence 2–10–2–10 and the process was monitored by QCM. For the in situ QMS studies, the TMA and water doses of the ALD Al₂O₃ overcoating cycles were divided into 10 × 0.5 s pulses to capture the temporal evolution of the gaseous products during each half ALD cycle. Nitrogen purge periods of 10 s were used after each TMA and water pulse. The QMS signals for all of the gaseous products were calibrated using standard gases

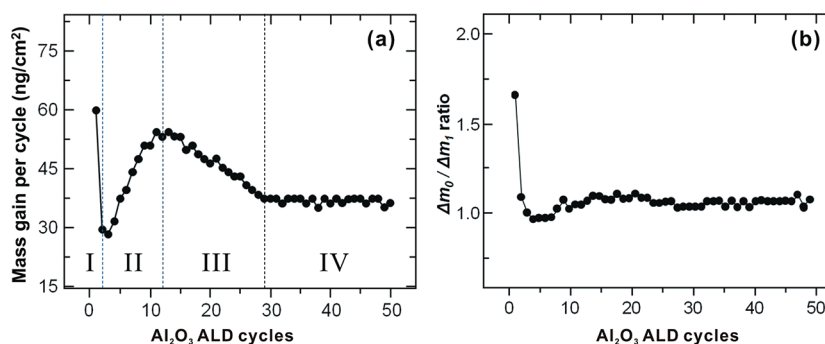


Figure 2. In situ QCM measurements of Al₂O₃ ALD on a Pd NP-coated sensor. (a) Al₂O₃ mass gain per cycle, where the growth can be divided into 4 regions as described in the text; (b) the $\Delta m_0/\Delta m_1$ step ratio for each cycle.

(1000 ppm of hydrogen, methane and ethane in nitrogen, Air Liquide).

Morphology of ALD Al₂O₃ Overcoated Pd NPs. To characterize the ultrathin ALD overcoatings on the Pd NPs, high resolution transmission electron microscopy (TEM) was performed using spherical Al₂O₃ powder (Al₂O₃ NanoDur, 99.5%, Alfa Aesar) as the starting support. About 600 mg of Al₂O₃ support was loaded into the ALD reactor. Four cycles of Pd ALD (300–300–300–300) were first performed after a 10 min ozone cleaning treatment and 20 min stabilization in the flow of nitrogen at 473 K.²⁸ Next, different numbers of ALD Al₂O₃ overcoating cycles were performed with the timing sequence (60–180–120–180).¹³ The ALD Al₂O₃ overcoated Pd samples were characterized using a JEOL JEM-2100F fast TEM system (NUANCE facility, Northwestern University) operated at 200 kV.

DFT Calculations. The thermodynamics of the surface species were obtained by performing periodic DFT calculations using the Vienna Ab initio Simulation Package (VASP).^{51–54} The ionic cores were treated with the projector augmented wave (PAW) method.^{55,56} The PW91 generalized gradient functional (GGA-PW91) functional was used to describe the electron exchange-correlation interactions.^{57,58}

The Pd nanoparticle surfaces were modeled using the idealized (111) and (211) facets to represent the terrace and the stepped regions, respectively. The Pd(111) slab consisted of a 3-layer, $p(3 \times 3)$ unit cell. The Pd(211) slab consisted of a 3-layer unit cell with three atoms included along the step edge. The top layer was allowed to relax in each case. A vacuum equivalent to five metal layers was used between successive metal slabs. The lattice constant was determined to be 3.95 Å, which compares well with both the experimental and theoretical bulk lattice values.^{59,60} The surface Brillouin zone was sampled with $4 \times 4 \times 1$ and $3 \times 3 \times 1$ k-point based on the Monkhorst-Pack sampling scheme for Pd(111) and Pd(211) respectively.⁶¹ The Kohn–Sham valence states were expanded in the plane wave basis sets up to 25 Ry (or 340 eV). The self-consistent iterations were converged with a criterion of 1×10^{-6} , and the ionic steps were converged to 0.02 eV/Å. The Methfessel-Paxton smearing scheme was used,⁶² with the Fermi population of the Kohn–Sham state being $k_B T = 0.2$ eV. The total energies were extrapolated to 0 eV. Dipole corrections were included in all cases. Zero-point energy corrections were not incorporated in this work. Gas phase energies were calculated in a box with dimensions of $17 \times 17 \times 18$ Å, using only the gamma-point. The Gaussian smearing parameter was 0.02 eV in this case. Spin polarization was included in both gas phase and surface calculations. Transition states (TSs) were calculated using the climbing-image nudged elastic band (CI-NEB) method.^{63,64} The dimer method was also used to further refine the determined transition states.⁶⁵ Each transition state was confirmed to have only one imaginary (negative) vibrational mode. The energy barriers were calculated using the lowest energy initial state configurations. If reactions involve more than one reactant, the barriers are reported with respect to the most stable reactant states at infinite separation from one another.

Free energies were determined with entropy corrections estimated assuming loss or gain of translational entropies of gas phase species as these species adsorb on, or desorb from, the surfaces at 473 K and standard pressure. The translational entropy correlations used for TMA, CH₄, C₂H₆, H₂O, and H₂ in this study were 0.84, 0.75, 0.79, 0.76, and 0.62 eV, respectively.

RESULTS

The Al₂O₃ ALD on high-density Pd NP-covered alumina surfaces was studied with in situ QCM and QMS, where 150 Pd ALD cycles were performed first to coat the entire ALD chamber and the quartz crystal surface with a high density of Pd NPs. Figure 2a shows the mass gain per cycle recorded using the QCM during the Al₂O₃ ALD and exhibits four distinct regions of growth. In region I, the first Al₂O₃ ALD cycle yielded a mass gain of ~60 ng/cm². In region II, the mass gain in the second cycle dramatically decreased to only 29 ng/cm² and was followed by a gradual increase to a maximum of 58 ng/cm² at about 13 cycles. Next, the mass gain gradually decreased to a value of 37 ng/cm² (region III) and remained at this steady state value (region IV). Figure 2b shows the ratio of the total mass gain in one ALD cycle to the mass gain after the TMA pulse ($\Delta m_0/\Delta m_1$). In the first Al₂O₃ ALD cycle, this mass ratio was 1.6, significantly higher than the expected value of ~1.1 in the subsequent cycles, which is the expected value for Al₂O₃ ALD on oxide surfaces (also seen in Figure S1 in the Supporting Information).^{44,66}

For the in situ QMS studies, we divided the TMA and H₂O exposures into ten pulses in each Al₂O₃ ALD cycle to investigate the detailed temporal evolution of the reaction products. Figure 3a shows an expanded view of the gaseous reaction products released during the first ALD cycle on the Pd NP surfaces. In this figure, the QMS signals for each species have been scaled by their experimentally determined calibration factors so that the traces represent the relative partial pressures for each species. Surprisingly, a small amount of C₂H₆ was observed (about 2.1%, $m/e = 30$) along with the dominant CH₄ product ($m/e = 16$) during the first TMA pulse. In the following nine TMA pulses, the C₂H₆ signals dramatically decreased to the noise level, and the CH₄ gradually decreased to a constant value consistent with the cracking pattern of the TMA. It was also surprising that during the H₂O pulses, a small amount of H₂ was formed ($m/e = 2$) along with the dominant CH₄ product, which both decreased to the noise level after the first and fourth H₂O pulses, respectively. Figure 3b shows a compressed view of the first 9 ALD Al₂O₃ cycles on the Pd NP surfaces and demonstrates that C₂H₆ was only observed during the first cycle, whereas H₂ was observed for about 7 cycles with

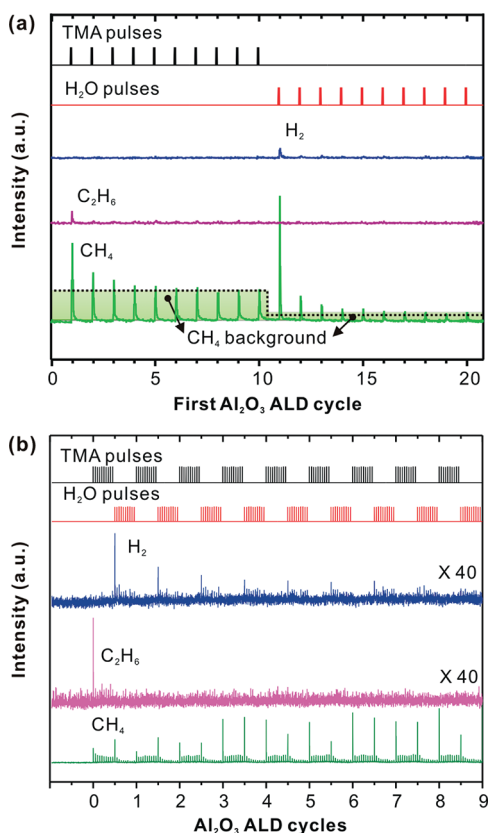


Figure 3. In situ QMS measurements of Al_2O_3 ALD performed after coating the inner surfaces of the ALD reactor with Pd NPs. The TMA and H_2O pulse sequences are indicated to correlate the QMS signals with the precursor exposures. (a) An expanded view of reaction products generated during the first ALD cycle. The green filled areas under the dashed lines designate the CH_4 background signals. (b) Reaction products formed during the first nine ALD Al_2O_3 cycles.

a gradually decreasing intensity. Meanwhile, the total CH_4 product ($\text{CH}_4_{\text{total}}$) in each cycle increased with increasing number of ALD cycles.

Figure 4 shows more clearly the evolution of the CH_4 QMS signals during the TMA and H_2O exposures during the Al_2O_3 ALD. The ratio of $\text{CH}_4_{\text{total}}/\text{CH}_4_{\text{TMA}}$ (the total CH_4 released divided by the amount released during the TMA pulse) in Figure 4a shows a steady state value of ~ 2 after ca. 5 cycles that is consistent with previous measurements and implies that $\sim 1/2$ of the CH_3 ligands are released during TMA

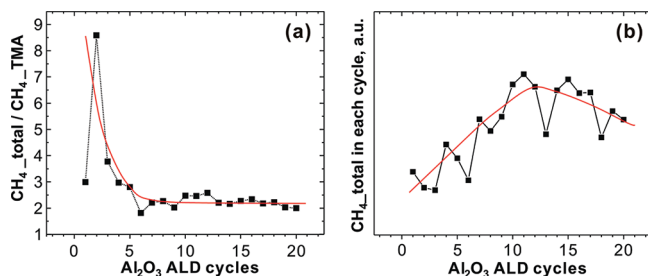


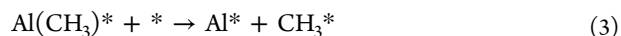
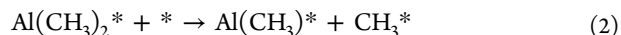
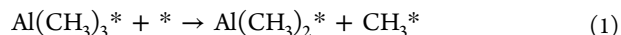
Figure 4. Summary plots of the in situ QMS measurements of Al_2O_3 ALD on Pd NP surfaces. (a) The ratio of the total CH_4 formed to the CH_4 formed during the TMA exposure in each ALD cycle; (b) the total amount of methane formed in each ALD cycle. The red curves are intended to guide the eye.

adsorption on the ALD Al_2O_3 surface (Figure 1).^{44,66} In contrast, higher mass ratios are seen in the initial 5 cycles, suggesting that more than 1/2 of the CH_3 ligands remain on the surface when TMA reacts on Pd. Figure 4b shows that the total amount of CH_4 released during each cycle gradually increased to a maximum at ~ 10 – 15 cycles and subsequently decreased. Since $\text{CH}_4_{\text{total}}$ is proportional to the amount of Al_2O_3 deposited, this observation is consistent with the QCM data in Figure 2a.

High-resolution TEM images provide direct evidence for the ALD Al_2O_3 overcoats on the Pd NPs (Figure 5). The Pd NPs formed using 4 ALD Pd cycles have a diameter of ~ 3 nm. Prior to the ALD Al_2O_3 overcoating, the NPs exhibit a sharp interface with the vacuum of the TEM environment (Figure 5a, inset). The thickness of the ALD Al_2O_3 overcoats grew linearly with the number of ALD cycles at a growth rate of 0.16 nm/cycle (Figure 5f). This value is consistent with the ALD Al_2O_3 on BN NPs reported in the literature,^{5,67} and the linear growth agrees well with our in situ QCM measurements (see Figure S2 in the Supporting Information). The detailed structure of the amorphous Al_2O_3 over layers, such as porosity, however, cannot be resolved by these TEM images.

The results of the DFT calculations are presented in Figure 6, which shows the free energy changes for TMA dissociative adsorption on Pd surfaces during the TMA pulse (Figure 6a), together with the hydroxylation of the Al during the subsequent water pulse (Figure 6b) calculated at 473 K and standard pressure. Gas phase TMA, a clean Pd surface (either Pd(111) or Pd(211)), and the adsorbed atomic H (1/9 ML H coverage) are used as the reference states.

On Pd(111), TMA adsorbs most strongly on the 3-fold (hcp) site (adsorption at fcc sites is only slightly less stable). Two of the Al–C bonds become elongated from 1.97 Å in the gas phase to 2.34 Å upon adsorption. The dissociation to dimethylaluminum (DMA, $\text{Al}(\text{CH}_3)_2^*$) and CH_3^* (on top sites), represented by eq 1, is 0.38 eV exothermic, with an energy barrier of 0.16 eV for the Al–C scission. DMA also prefers the hcp site (again, fcc adsorption is only slightly less stable) in a tilted position with one of the Al–C bonds elongated to 2.36 Å (see Figure 1S in the Supporting Information for the schematic geometries). DMA can further dissociate into AlCH_3^* (methylaluminum, MA, which also has a slight preference for hcp adsorption) and CH_3^* , which is 0.37 eV exothermic (eq 2 below). The energy barrier for the second Al–C bond scission is also 0.16 eV. We also note that a direct, concerted pathway for TMA conversion to MA, with a single transition state and a low barrier of 0.11 eV, also exists, as indicated by the dashed line between states 2 and 4. It is not favorable to further convert MA to Al^* and CH_3^* (eq 3) on terrace sites, a process which is endothermic by 0.85 eV with an energy barrier of 1.37 eV.



Cleavage of Al–C bonds in $\text{Al}(\text{CH}_3)_3^*$ and $\text{Al}(\text{CH}_3)_2^*$ is more thermodynamically favorable on the step site of a Pd(211) surface. Both $\text{Al}(\text{CH}_3)_3^*$ and $\text{Al}(\text{CH}_3)_2^*$ are very unstable on the steps; in fact, TMA directly dissociates into $\text{Al}(\text{CH}_3)^*$ at the step edge site via the path indicated by the dashed line in Figure 6 a. Further, the predicted barrier to break an Al–C

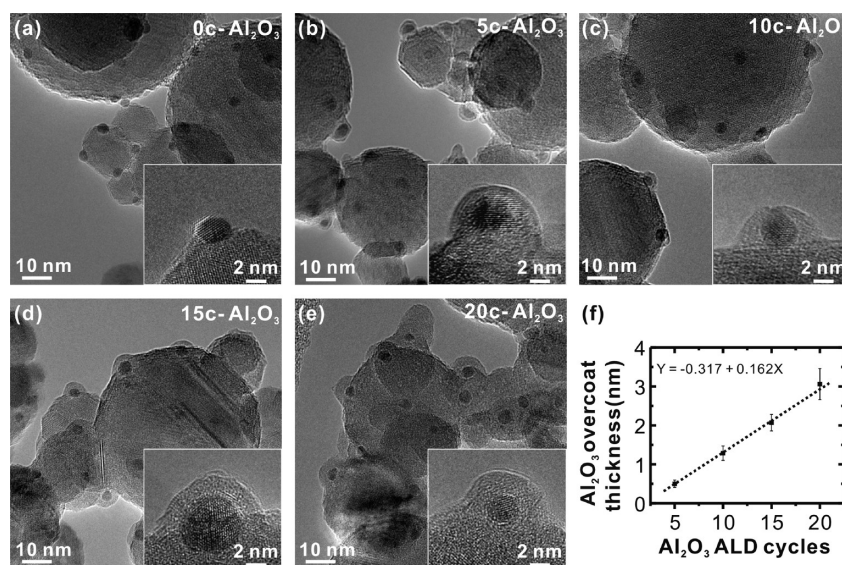


Figure 5. TEM images of spherical alumina supported Pd catalysts with different numbers of Al_2O_3 ALD overcoating cycles (insets show higher magnification images). (a) 0 cycle Al_2O_3 ; (b) 5 cycles Al_2O_3 ; (c) 10 cycles Al_2O_3 ; (d) 15 cycles Al_2O_3 ; (e) 20 cycles Al_2O_3 ; (f) thickness of Al_2O_3 overcoats versus ALD cycles.

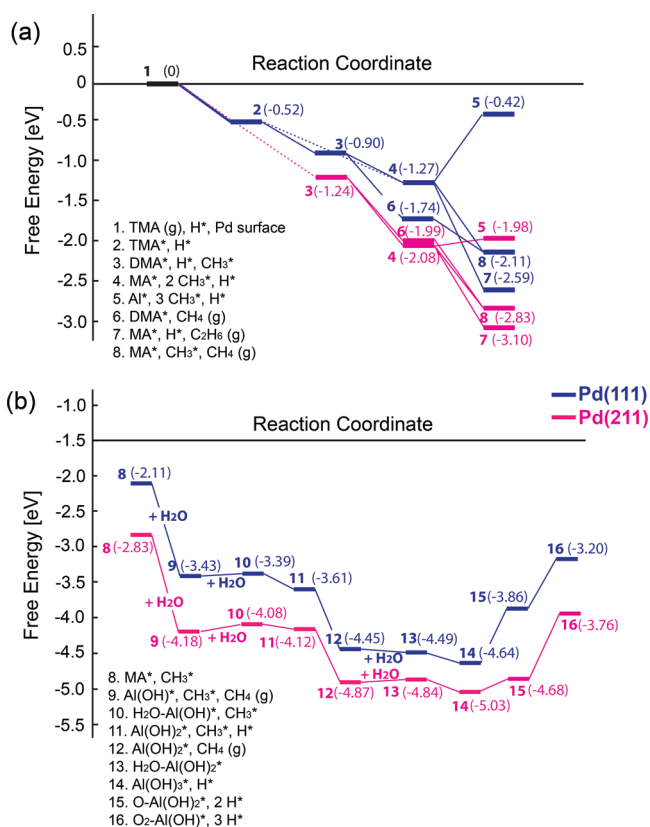


Figure 6. Free energy diagrams of surface species formed during (a) exposure to TMA and subsequently to (b) water on Pd(111) (dark blue) and Pd(211) (magenta) surfaces calculated at 473 K and 1 atm. The gas phase TMA, clean surface, and a preadsorbed H atom are used as the reference state (black bar at 0 eV). Energy barriers are not shown in the diagrams. Dashed lines in panel a indicate the formation of MA from TMA via two simultaneous Al–C bond scissions. Schematic representations of the surface geometries for these species are shown in Figure S3 in the Supporting Information.

bond in DMA (eq 2) is also very low, resulting in stable $\text{Al}(\text{CH}_3)^*$ (adsorbed on the step edge) and CH_3^* (also preferentially adsorbed on the step edge). In contrast to Pd(111), the relatively small free energy increase (~ 0.1 eV) for reaction 3 suggests that some $\text{Al}(\text{CH}_3)^*$ might further dissociate into Al^* and CH_3^* on step edges; the barrier for this process is 0.43 eV. The free energy of $\text{Al}(\text{CH}_3)^*$ adsorption on the step edge site is lower than that on Pd(111) by approximately 0.81 eV. The DFT results thus demonstrate that the step sites are much more thermodynamically favorable for TMA dissociative adsorption than are the Pd(111) terraces. These calculations are consistent with our previous CO chemisorption measurements showing that the first cycle of ALD Al_2O_3 preferentially nucleated at the low-coordinated Pd NP sites.¹³

The dissociated methyl groups, CH_3^* , bind relatively strongly to Pd(111) and Pd(211), with binding energies of -1.88 and -2.03 eV, respectively, calculated relative to a gas phase methyl radical and a clean palladium surface. It is thus possible that these species will remain on the surface and become abundant under the conditions used in our study. Literature results suggest that additional decomposition of the CH_3^* species is not expected. Adsorbed CH_3^* on Pd(111) was found experimentally to be thermally stable to at least 440 K, as shown in methanol decomposition studies.^{68,69} Additionally, DFT calculations by Paul and Sautet on CH_x^* fragments on Pd(111) surfaces showed an endothermic path for the decompositions of CH_3^* .⁷⁰

The DFT results can be used to rationalize the gas phase products observed by in situ QMS. Methane released during the TMA exposures (Figure 3) results from CH_3^* combining with preadsorbed H^* (eq 4, see states 6 and 8 in Figure 6a). The ethane seen during the first TMA pulse could result from the coupling of two adjacent CH_3^* species according to eq 5 (corresponding to state 7 in Figure 6a). The formation of methane and ethane would be assisted by the entropy gained upon desorption. The relatively small ratio of ethane/methane observed by in situ QMS is likely due to the higher energy barriers for C–C bond formation (1.58 and 1.02 eV on

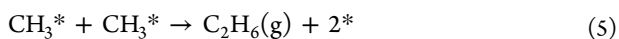
Pd(111) and Pd(211), respectively, see Table 1) compared to C–H bond formation (with energy barriers of 0.67 and 0.63 eV

Table 1. Activation Energy Barriers (in eV) for Methane, Ethane Formation, and Water Dissociation on Pd(111) and Pd(211) Surfaces (without zero-point energy corrections)^a

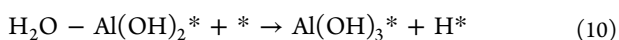
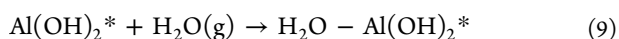
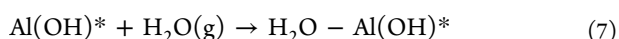
	Pd(111)	Pd(211)
$\text{CH}_3^* + \text{H}^* \rightarrow \text{CH}_4(\text{g})$	0.67	0.48
$\text{CH}_3^* + \text{CH}_3^* \rightarrow \text{C}_2\text{H}_6(\text{g})$	1.58	1.02
Water Dissociation: $\text{H}_2\text{O}^* \rightarrow \text{H}^* + \text{OH}^*$		
	Pd(111)	Pd(211)
on clean surface	1.05	1.19
In $\text{H}_2\text{O}-\text{Al}(\text{OH})^*$	0.58	0.52
In $\text{H}_2\text{O}-\text{Al}(\text{OH})_2^*$	0.58	0.39

^aAssociative desorption barriers are referenced to the adsorbed reactants at infinite separation from one another.

on Pd(111) and Pd(211), respectively, in good agreement with literature values.⁷¹). Nevertheless, this small amount of ethane does support the existence of a large concentration of CH_3^* on the Pd surface from TMA dissociation.^{72–74} Compared to CH_3^* , the coverages for both CH_x^* ($x = 0–2$) fragments and H^* should be low because no hydrogen was seen by in situ QMS during the TMA exposures, and because the decomposition of CH_3^* is suggested to be endothermic⁷⁰ (see also discussion above). The CH_3^* radicals that remain on the surface after the TMA exposure would act as a poison to block further TMA adsorption.



Below, we briefly summarize the DFT-determined thermodynamics of the subsequent reactions of $\text{Al}(\text{CH}_3)^*$ and CH_3^* with water or water derivatives during the water exposure to the Pd(111) and Pd(211) surfaces (Figure 6b). The adsorbed structures are schematically represented in Figure S3 in the Supporting Information. The transformation of $\text{Al}(\text{CH}_3)^*$ into $\text{Al}(\text{OH})^*$, accompanied by the formation of methane is represented by eq 6. The free energy change of this reaction is highly exothermic, by ~ 1.3 eV, on both Pd(111) and Pd(211) surfaces. Further reactions with water to insert hydroxyls and form $\text{Al}(\text{OH})_2^*$ and $\text{Al}(\text{OH})_3^*$ (eqs 7–10), are found to be thermodynamically favorable on both Pd(111) and Pd(211) surfaces. In fact, $\text{Al}(\text{OH})_3^*$ was found to be the most thermodynamically stable intermediate on the Pd surfaces (Figure 6b). Reactions involving further O–H bond cleavage to form $\text{O}_x\text{Al}(\text{OH})_{3-x}^*$ species ($x = 1–2$) are endothermic.



As shown in eqs 8 and 10, atomic H^* is produced during the hydration of the $\text{Al}(\text{OH})_x^*$ species ($x = 1, 2$). We note that this

mechanism for cleaving H–OH bonds in water has a lower barrier than direct dissociation of water on palladium surfaces (see Table 1 for comparison of water dissociation on clean surface and in $\text{Al}(\text{OH})_x^*$ complexes). These H^* could react with either CH_3^* species to release methane, (eq 4), or combine with an additional H^* to form molecular hydrogen (eq 11). These results are consistent with the observation of methane and small amount of hydrogen during the water pulses during the in situ QMS experiments (Figure 3).

The thermochemistry for the reaction of water with the $\text{Al}(\text{CH}_3)^*$ and CH_3^* species on the planar (111) and stepped (211) are qualitatively similar in that the substitution and additional hydration reactions of $\text{Al}(\text{OH})^*$ are all exothermic. However, these reactions are much more thermodynamically favorable on the step sites of the Pd(211) surfaces.

DISCUSSION

In situ QCM and QMS are valuable tools for exploring the surface chemistry during ALD processes. These techniques are especially useful in our study for monitoring the initial cycles of Al_2O_3 ALD where the TMA and water interact directly with the Pd surface. In our experiments, the 150-cycle Pd ALD pretreatment yielded an average Pd coverage of ~ 6 ML (~ 14.7 Å). Previous scanning electron microscopy (SEM) studies demonstrated that this 6 ML coating is comprised of densely packed, discrete Pd NPs.⁵⁰ This morphology will increase the Pd surface roughness compared to a smooth film as illustrated by the schematic model in Figure 7a. If the Al_2O_3 nucleated uniformly on this rough Pd surface, the QCM would show a high initial mass gain per cycle that gradually decreased to the expected steady-state value of 37 ng/cm^2 per cycle as the nanoscale roughness was eventually filled by the ALD Al_2O_3 film. However, Figure 2a shows a much different behavior. The Al_2O_3 mass gain during the first cycle was 60 ng/cm^2 , significantly higher than the steady-state value. Next, the mass gain increased gradually from an initial value of ~ 29 ng/cm^2 (below the steady state value), reached a maximum at ~ 13 cycles, and then decreased to the steady-state value.

The evolution in QCM mass changes can be explained by incomplete Al_2O_3 nucleation and changes in substrate surface area. The behavior in regions II–IV of Figure 2a resembles “type-2” substrate-inhibited ALD in which growth initiates at discrete sites forming islands that eventually coalesces to form a continuous film.^{4,75} Here the much more pronounced maximum value at ~ 13 cycles compared to that in the “type-2” model is a consequence of the rough starting Pd surface in our case (Figure 7a). This similarity indicates that the Al_2O_3 initiates nonuniformly on the Pd surface (Figure 7b, c) in agreement with our previous DRIFTS studies of CO chemisorption that showed preferential nucleation in the first ALD Al_2O_3 cycles only at the low-coordination Pd NP sites.¹³ The DFT calculations support this interpretation since the free energy for MA adsorption is ~ 0.81 eV stronger on the Pd(211) step surface than on the Pd(111) hcp sites.

With increasing ALD cycles, the Al_2O_3 patches grow in 3 dimensions, accompanied by the continuous $\text{Al}(\text{OH})_3^*$ nucleation (Figure 7d). The continuous nucleation in this Region II will be discussed later. Consequently, the surface area increases causing the mass gain per cycle to grow (Region II in Figure 2a) and reach a maximum as the Al_2O_3 patches begin to coalesce. Afterward, the Al_2O_3 growth changes to a layer-by-layer growth mode. Meanwhile, the growth per cycle decreases as the alumina patches merge into a continuous film (Figure 2a,

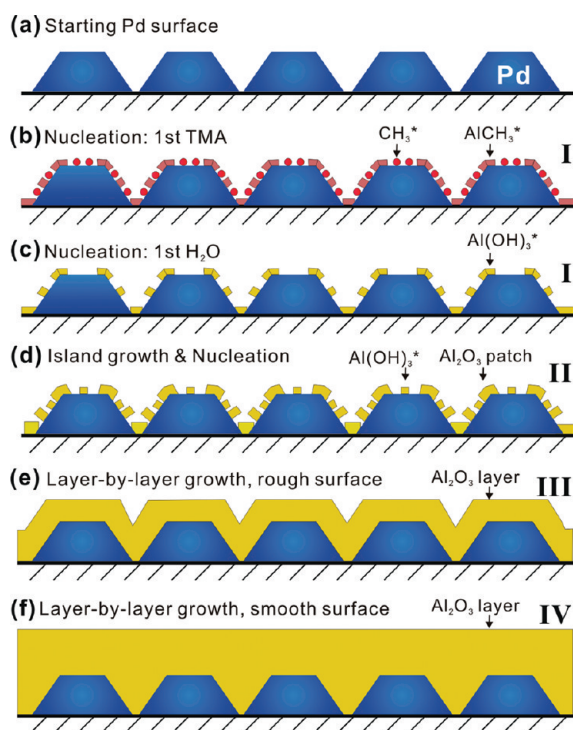


Figure 7. Schematic illustration of Al_2O_3 ALD on a surface coated with Pd NPs. The Roman numerals correspond to the labeled regimes in Figure 2a. (a) Initial surface is decorated with a high density of Pd NPs that increase the surface roughness; (b) Region I, nucleation through the TMA dissociative adsorption on the Pd corner and edge sites, forming $\text{Al}(\text{CH}_3)^*$ and CH_3^* species; (c) Region I, first H_2O exposure to the $\text{Al}(\text{CH}_3)^*$ and CH_3^* terminated Pd surface, forming $\text{Al}(\text{OH})_3^*$ species; (d) Region II, island growth in three dimensions as well as additional nucleation; (e) Region III, layer-by-layer growth occurs and develops after Al_2O_3 patches coalesce to form a continuous film on the rough Pd surface; (f) Region IV, layer by layer growth, where initial roughness generated by the Pd NPs has vanished so that the surface is smooth.

region III and Figure 7e), and eventually the roughness disappears so that the mass gain in each cycle reaches a constant value (Figure 2a, region IV, and Figure 7f).

Overall, the in situ QMS data in Figure 4 support the island coalescence mechanism described above. Beyond ~ 5 cycles, the CH_4 product ratio of ~ 2 (Figure 4a) is consistent with the conventional mechanism for Al_2O_3 ALD where $1/2$ of the CH_3^* species are lost during each half-reaction (Figure 1). Furthermore, the overall increase and then decrease in the total CH_4 QMS signals (Figure 4b) match well with the QCM data (Figure 2a) after the first ALD cycle. However, there is an apparent discrepancy in that the QCM mass increase during the first ALD cycle on Pd is anomalously large while the corresponding CH_4 QMS signal is nominal. Furthermore, the QCM mass ratio is anomalously high during the first cycle (Figure 2b), and the QMS mass ratio remains above the steady state value for the first ~ 5 cycles. These apparent discrepancies, as well as the unusual gas phase products observed during the initial stages of Al_2O_3 ALD on Pd, can be explained by the unique chemistry for the TMA and water reactions on the Pd surface. As suggested by the DFT calculations, TMA can nucleate on Pd surfaces through Al–C bond scission (eqs 1–2) without the need for surface hydroxyl species. The observed ethane directly supports TMA dissociative adsorption on the Pd, since ethane can form through the coupling of two CH_3^* at

higher coverages.^{72–74} This is also consistent with the CH_4 total to CH_4 TMA ratio showing higher values in the first five cycles than the remaining cycles (Figure 4a). On the other hand, the DFT calculations showed that the energy barriers to form C_2H_6 on the Pd(211) and Pd(111) surfaces are 1.02 and 1.58 eV, respectively, (Table 1), suggesting that the C_2H_6 product observed in the first cycle is likely generated through the coupling of two adjacent CH_3^* species at the under-coordinated Pd sites rather than on the Pd(111) terraces. Therefore, it is not a surprise that we observed C_2H_6 only in the first cycle (Figure 3b), because the under-coordinated Pd sites become occupied by $\text{Al}(\text{OH})_3^*$ species after the first ALD Al_2O_3 cycle.

The significantly higher $\Delta m_0/\Delta m_1$ mass ratio of 1.6 in the first cycle (Figure 2b) indicates that the surface species produced when water interacts with the TMA-treated Pd surface are different compared to TMA-treated oxide surfaces. As stated above, $\text{Al}(\text{OH})_3^*$ is the most stable intermediate species identified by DFT calculations. Therefore, the water exposure in the first ALD cycle should convert the $\text{Al}(\text{CH}_3)^*$ into $\text{Al}(\text{OH})_3^*$ rather than $\text{Al}(\text{OH})^*$, according to eqs 6–10. The QCM step ratio resulting from this complete hydroxylation will depend on the number of CH_3^* species remaining on the Pd after the TMA exposure: $\Delta m_0/\Delta m_1 = 2.00$, 1.41, and 1.08 for 1, 2, and 3 CH_3^* species, respectively. Our in situ QCM results showed a ratio of 1.6, suggesting ~ 2 CH_3^* species remain on the Pd surface. Table 1 lists the energy barriers for water dissociation on clean Pd as well as in the presence of $\text{Al}(\text{OH})^*$ and $\text{Al}(\text{OH})_2^*$ complexes. The O–H bond cleavage in water becomes significantly easier in the presence of under-coordinated Al species. These modeling results provide an explanation for why H_2 was only observed during the initial pulses of the H_2O exposures (Figure 3). The H_2 is produced by the recombinative desorption of H^* species (eq 11). These H^* species form through the dissociation of H_2O on under-coordinated Al species (eqs 7–10) which are most abundant near the beginning of the H_2O exposures.

The inhibited Al_2O_3 growth following the first ALD cycle is likely caused by a large concentration of CH_3^* species that block potential TMA adsorption sites. This site blocking is only temporary, since the CH_3^* species are released as CH_4 during the following water dose, so that the Pd surface becomes exposed again for reaction with TMA in the next cycle (Figure 7b and c). This self-poisoning and self-cleaning process continues for ~ 7 cycles, as demonstrated by the persistent but gradually decreasing H_2 production (Figure 3b). This mechanism will allow the continuous nucleation of new Al_2O_3 islands on the exposed Pd sites as well as the growth of existing Al_2O_3 patches in 3 dimensions (Figure 7d). As a consequence, the Al_2O_3 will grow as a discontinuous film rather than a continuous, pinhole-free coating typical for ALD. Our recent CO chemisorption studies on ALD Al_2O_3 -coated Pd showed that bare Pd sites remained even after 8 cycles of ALD Al_2O_3 overcoating.¹³ In agreement with this finding, the H_2 signals that persist for ~ 7 cycles suggest that the Al_2O_3 overcoat is sufficiently porous to allow water to access the Pd NP surfaces (Figure 8). In contrast to our results on Pd, Al_2O_3 ALD on silver uniformly blankets the metal surface.^{33,49} This behavior is likely due to the weaker bonding of methyl species on Ag versus Pd, resulting in far fewer CH_3^* inhibitors on the Ag.

Recently, Weimer et al. synthesized aluminum alkoxide (alucone) hydride films by molecular layer deposition using TMA and ethylene glycol (EG) over Pt/ SiO_2 catalysts. Upon

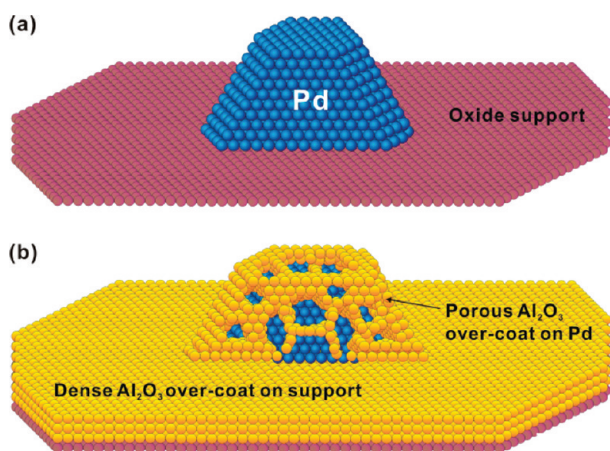


Figure 8. Schematic illustration of porous ALD Al_2O_3 overcoat on Pd NP. (a) Oxide-supported Pd catalyst; (b) dense Al_2O_3 film on oxide support and porous Al_2O_3 overcoat on Pd NP formed by ALD.

annealing to decompose the alucone, the resulting Al_2O_3 films were found to be highly porous.³⁴ A direct comparison between the porosity of the ALD Al_2O_3 overlayers produced in this study with those of Weimer et al. would require further investigation.

It is remarkable in our studies that the Pd NPs overcoated with up to 7–8 cycles remain accessible to small reagent gases like water, CO, and methanol, even though TEM measurements show these particles to be embedded in a 1 nm coating. Furthermore, porosity can be induced into much thicker ALD Al_2O_3 overcoats on Pd NPs surface through temperature treatment or long-term reaction at elevated temperatures, which was indicated by the gain in CO chemisorption capacity on the used catalysts.^{13,17} For example, we recently showed that when a Pd/ Al_2O_3 catalyst with 45 cycles of ALD Al_2O_3 overcoat was treated at 973 K in an oxygen environment, the Pd surfaces became accessible to reagent gases through the development of microporosity (~ 2 nm) inside the Al_2O_3 layer.¹⁷ Through overcoating and annealing, it might be possible to tune the activity and selectivity of Pd catalysts by controlling the porosity of the Al_2O_3 (Figure 8).^{13,17}

CONCLUSIONS

We have investigated the growth mechanism of Al_2O_3 ALD using TMA and water on Pd NPs surfaces by combining in situ QCM, in situ QMS, and TEM experimental studies with DFT calculations. Both QCM and QMS presented a consistent picture that Al_2O_3 only grows on certain portions of the Pd NPs rather than forming a continuous coating in the initial cycles. The high CH_4 -total to CH_4 -TMA ratio and the production of ethane suggest that the coverage of CH_3^* should be high after the TMA pulse. The hydrogen product, observed during the water exposures in the first ~ 7 cycles, suggests that the ALD Al_2O_3 layer is porous, consistent with our previous CO chemisorption studies. A mechanism is proposed for TMA dissociative adsorption and hydration of TMA intermediates based on DFT calculations. Thermodynamic analysis shows that the TMA dissociation is more favored on the stepped sites than the terrace sites, suggesting that low-coordination Pd sites may facilitate TMA nucleation in the first ALD cycle. Moreover, DFT calculations also show that the hydration product $\text{Al}(\text{OH})_3^*$ is more thermodynamically favorable than $\text{Al}(\text{OH})^*$ during the water pulses, explaining the anomalously

high $\Delta m_0/\Delta m_1$ mass ratio observed during the first cycle by in situ QCM.

ASSOCIATED CONTENT

Supporting Information

Additional figures (PDF). This material is available free of charge via the Internet at <http://pubs.acs.org>.

AUTHOR INFORMATION

Corresponding Author

*E-mail: jelam@anl.gov.

Notes

The authors declare no competing financial interest.

ACKNOWLEDGMENTS

J.W.E., J.P.G., B.L., and J.L. were supported as part of the Institute for Atom-efficient Chemical Transformations (IACT), an Energy Frontier Research Center funded by the U.S. Department of Energy (DOE), Office of Science, Office of Basic Energy Science. Z.F. and M.J.B. thank the support of the Institute for Catalysis and Energy Processes (U.S. Department of Energy Grant, DE-FG02-03ER15457). P.C.S. and Y.L. acknowledge support from the U.S. Department of Energy, BES-HFI, Chemical Sciences, under Contract DE-AC-02-06CH11357. Use of the Center for Nanoscale Materials was supported by the U.S. Department of Energy, Office of Science, Office of Basic Energy Science, under Contract DE-AC02-06CH11357. We also acknowledge grants of computer time from EMSL, a national scientific user facility located at Pacific Northwest National Laboratory, and the Argonne Laboratory Computing Resource Center (LCRC), and resources of the National Energy Research Scientific Computing Center (NERSC).

REFERENCES

- Ritala, M. *Appl. Surf. Sci.* **1997**, *112*, 223.
- Suntola, T.; Hyvarinen, J. *Annu. Rev. Mater. Sci.* **1985**, *15*, 177.
- George, S. M. *Chem. Rev.* **2010**, *110*, 111.
- Puurunen, R. L. *J. Appl. Phys.* **2005**, *97*, 121301.
- Ferguson, J. D.; Weimer, A. W.; George, S. M. *Thin Solid Films* **2000**, *371*, 95.
- Libera, J. A.; Elam, J. W.; Pellin, M. J. *Thin Solid Films* **2008**, *516*, 6158.
- Lim, B. S.; Rahtu, A.; Gordon, R. G. *Nat. Mater.* **2003**, *2*, 749.
- Elam, J. W.; Xiong, G.; Han, C. Y.; Wang, H. H.; Birrell, J. P.; Welp, U.; Hryn, J. N.; Pellin, M. J.; Baumann, T. F.; Poco, J. F.; Satcher, J. H. *J. Nanomater.* **2006**, *2006*, 1.
- Elam, J. In *Atomic Layer Deposition of Nanostructured Materials*; Pinna, N., Knez, M., Eds.; Wiley-VCH: Weinheim, Germany, 2012; p 227.
- Lei, Y.; Mehmood, F.; Lee, S.; Greeley, J.; Lee, B.; Seifert, S.; Winans, R. E.; Elam, J. W.; Meyer, R. J.; Redfern, P. C.; Teschner, D.; Schlogl, R.; Pellin, M. J.; Curtiss, L. A.; Vajda, S. *Science* **2010**, *328*, 224.
- Enterkin, J. A.; Setthapun, W.; Elam, J. W.; Christensen, S. T.; Rabuffetti, F. A.; Marks, L. D.; Stair, P. C.; Poepplmeier, K. R.; Marshall, C. L. *ACS Catal.* **2011**, *1*, 629.
- Feng, H.; Elam, J. W.; Libera, J. A.; Setthapun, W.; Stair, P. C. *Chem. Mater.* **2010**, *22*, 3133.
- Feng, H.; Lu, J. L.; Stair, P. C.; Elam, J. W. *Catal. Lett.* **2011**, *141*, 512.
- Christensen, S. T.; Feng, H.; Libera, J. L.; Guo, N.; Miller, J. T.; Stair, P. C.; Elam, J. W. *Nano Lett.* **2010**, *10*, 3047.
- Feng, H.; Elam, J. W.; Libera, J. A.; Pellin, M. J.; Stair, P. C. *J. Catal.* **2010**, *269*, 421.

- (16) King, J. S.; Wittstock, A.; Biener, J.; Kucheyev, S. O.; Wang, Y. M.; Baumann, T. F.; Giri, S. K.; Hamza, A. V.; Baeumer, M.; Bent, S. F. *Nano Lett.* **2008**, *8*, 2405.
- (17) Lu, J. L.; Fu, B. S.; Kung, M. C.; Xiao, G. M.; Elam, J. W.; Kung, H. H.; Stair, P. C. *Science* **2012**, *335*, 1205.
- (18) Martinson, A. B. F.; Elam, J. W.; Pellin, M. J. *Appl. Phys. Lett.* **2009**, *94*, 123107.
- (19) Libera, J. A.; Hryn, J. N.; Elam, J. W. *Chem. Mater.* **2011**, *23*, 2150.
- (20) Nanu, M.; Schoonman, J.; Goossens, A. *Adv. Mater.* **2004**, *16*, 453.
- (21) Chen, Y. W.; Prange, J. D.; Duhnen, S.; Park, Y.; Gunji, M.; Chidsey, C. E. D.; McIntyre, P. C. *Nat. Mater.* **2011**, *10*, 539.
- (22) Scott, I. D.; Jung, Y. S.; Cavanagh, A. S.; An, Y. F.; Dillon, A. C.; George, S. M.; Lee, S. H. *Nano Lett.* **2011**, *11*, 414.
- (23) Chao, C. C.; Hsu, C. M.; Cui, Y.; Prinz, F. B. *ACS Nano* **2011**, *5*, 5692.
- (24) Adamczyk, N. M.; Dameron, A. A.; George, S. M. *Langmuir* **2008**, *24*, 2081.
- (25) Du, Y.; George, S. M. *J. Phys. Chem. C* **2007**, *111*, 8509.
- (26) Mayer, T. M.; Elam, J. W.; George, S. M.; Kotula, P. G.; Goeke, R. S. *Appl. Phys. Lett.* **2003**, *82*, 2883.
- (27) Davidson, B. D.; Seghete, D.; George, S. M.; Bright, V. M. *Sens. Actuators, A* **2011**, *166*, 269.
- (28) Lu, J. L.; Stair, P. C. *Langmuir* **2010**, *26*, 16486.
- (29) Feng, H.; Elam, J. W.; Libera, J. A.; Stair, P. C.; Miller, J. T. *ACS Catal.* **2011**, *1*, 665.
- (30) Lu, J. L.; Stair, P. C. *Angew. Chem., Int. Ed.* **2010**, *49*, 2547.
- (31) Christensen, S. T.; Elam, J. W.; Rabuffetti, F. A.; Ma, Q.; Weigand, S. J.; Lee, B.; Seifert, S.; Stair, P. C.; Poeppelmeier, K. R.; Hersam, M. C.; Bedzyk, M. J. *Small* **2009**, *5*, 750.
- (32) Ma, Z.; Brown, S.; Howe, J. Y.; Overbury, S. H.; Dai, S. J. *Phys. Chem. C* **2008**, *112*, 9448.
- (33) Zhang, X. Y.; Zhao, J.; Whitney, A. V.; Elam, J. W.; Van Duyne, R. P. *J. Am. Chem. Soc.* **2006**, *128*, 10304.
- (34) Liang, X. H.; Li, J. H.; Yu, M.; McMurray, C. N.; Falconer, J. L.; Weimer, A. W. *ACS Catal.* **2011**, *1*, 1162.
- (35) Joo, S. H.; Park, J. Y.; Tsung, C. K.; Yamada, Y.; Yang, P. D.; Somorjai, G. A. *Nat. Mater.* **2009**, *8*, 126.
- (36) Ott, L. S.; Finke, R. G. *Coord. Chem. Rev.* **2007**, *251*, 1075.
- (37) Seipenbusch, M.; Binder, A. *J. Phys. Chem. C* **2009**, *113*, 20606.
- (38) Park, J. N.; Forman, A. J.; Tang, W.; Cheng, J. H.; Hu, Y. S.; Lin, H. F.; McFarland, E. W. *Small* **2008**, *4*, 1694.
- (39) Takenaka, S.; Matsumori, H.; Nakagawa, K.; Matsune, H.; Tanabe, E.; Kishida, M. *J. Phys. Chem. C* **2007**, *111*, 15133.
- (40) Scott, R. W. J.; Sivadinarayana, C.; Wilson, O. M.; Yan, Z.; Goodman, D. W.; Crooks, R. M. *J. Am. Chem. Soc.* **2005**, *127*, 1380.
- (41) Arnal, P. M.; Comotti, M.; Schuth, F. *Angew. Chem., Int. Ed.* **2006**, *45*, 8224.
- (42) Ott, A. W.; Klaus, J. W.; Johnson, J. M.; George, S. M. *Thin Solid Films* **1997**, *292*, 135.
- (43) Dillon, A. C.; Ott, A. W.; Way, J. D.; George, S. M. *Surf. Sci.* **1995**, *322*, 230.
- (44) Rahtu, A.; Alaranta, T.; Ritala, M. *Langmuir* **2001**, *17*, 6506.
- (45) Juppo, M.; Rahtu, A.; Ritala, M.; Leskela, M. *Langmuir* **2000**, *16*, 4034.
- (46) Elam, J. W.; Groner, M. D.; George, S. M. *Rev. Sci. Instrum.* **2002**, *73*, 2981.
- (47) Groner, M. D.; Fabreguette, F. H.; Elam, J. W.; George, S. M. *Chem. Mater.* **2004**, *16*, 639.
- (48) Whitney, A. V.; Elam, J. W.; Stair, P. C.; Van Duyne, R. P. *J. Phys. Chem. C* **2007**, *111*, 16827.
- (49) Whitney, A. V.; Elam, J. W.; Zou, S. L.; Zinovev, A. V.; Stair, P. C.; Schatz, G. C.; Van Duyne, R. P. *J. Phys. Chem. B* **2005**, *109*, 20522.
- (50) Elam, J. W.; Zinovev, A.; Han, C. Y.; Wang, H. H.; Welp, U.; Hryn, J. N.; Pellin, M. J. *Thin Solid Films* **2006**, *515*, 1664.
- (51) Kresse, G.; Hafner, J. *Phys. Rev. B* **1993**, *47*, 558.
- (52) Kresse, G.; Hafner, J. *Phys. Rev. B* **1994**, *49*, 14251.
- (53) Kresse, G.; Furthmuller, J. *Phys. Rev. B* **1996**, *54*, 11169.
- (54) Kresse, G.; Furthmuller, J. *Comput. Mater. Sci.* **1996**, *6*, 15.
- (55) Blochl, P. E. *Phys. Rev. B* **1994**, *50*, 17953.
- (56) Kresse, G.; Joubert, D. *Phys. Rev. B* **1999**, *59*, 1758.
- (57) Perdew, J. P.; Chevary, J. A.; Vosko, S. H.; Jackson, K. A.; Pederson, M. R.; Singh, D. J.; Fiolhais, C. *Phys. Rev. B* **1992**, *46*, 6671.
- (58) Perdew, J. P.; Chevary, J. A.; Vosko, S. H.; Jackson, K. A.; Pederson, M. R.; Singh, D. J.; Fiolhais, C. *Phys. Rev. B* **1993**, *48*, 4978.
- (59) Kittel, C. *Introduction to Solid State Physics*; 7th ed.; John Wiley & Sons: New York, 1996; p 673.
- (60) Loffreda, D.; Simon, D.; Sautet, P. *Chem. Phys. Lett.* **1998**, *291*, 15.
- (61) Monkhorst, H. J.; Pack, J. D. *Phys. Rev. B* **1976**, *13*, 5188.
- (62) Methfessel, M.; Paxton, A. T. *Phys. Rev. B* **1989**, *40*, 3616.
- (63) Henkelman, G.; Jonsson, H. *J. Chem. Phys.* **2000**, *113*, 9978.
- (64) Henkelman, G.; Johannesson, G.; Jonsson, H.; Kluwer Academic: New York, 2000, p 269.
- (65) Henkelman, G.; Jonsson, H. *J. Chem. Phys.* **1999**, *111*, 7010.
- (66) Puurunen, R. L. *J. Appl. Phys.* **2005**, *97*, 121301.
- (67) McCormick, J. A.; Rice, K. P.; Paul, D. F.; Weimer, A. W.; George, S. M. *Chem. Vap. Dep.* **2007**, *13*, 491.
- (68) Kruse, N.; Rebholz, M.; Matolin, V.; Chuah, G. K.; Block, J. H. *Surf. Sci.* **1990**, *238*, L457.
- (69) Levis, R. J.; Jiang, Z. C.; Winograd, N. *J. Am. Chem. Soc.* **1989**, *111*, 4605.
- (70) Paul, J. F.; Sautet, P. *J. Phys. Chem. B* **1998**, *102*, 1578.
- (71) Liu, Z. P.; Hu, P. *J. Am. Chem. Soc.* **2003**, *125*, 1958.
- (72) Marsh, A. L.; Becraft, K. A.; Somorjai, G. A. *J. Phys. Chem. B* **2005**, *109*, 13619.
- (73) Fairbrother, D. H.; Peng, X. D.; Viswanathan, R.; Stair, P. C.; Trenary, M.; Fan, J. *Surf. Sci.* **1993**, *285*, L455.
- (74) Fuhrmann, T.; Kinne, M.; Trankenschuh, B.; Papp, C.; Zhu, J. F.; Denecke, R.; Steinruck, H. P. *New J. Phys.* **2005**, *7*.
- (75) Puurunen, R. L.; Vandervorst, W. *J. Appl. Phys.* **2004**, *96*, 7686.